Microstructure and properties of a vacuum tempered glass with low-temperature sintered silver paste

Qin Sun (zhuwenbo@hit.edu.cn)
Harbin Institute of Technology Shenzhen
Guoji Sun
Harbin Institute of Technology Shenzhen
Yihan Liu
Harbin Institute of Technology Shenzhen
Yufeng Li
Harbin Institute of Technology Shenzhen
Hongtao Chen
Harbin Institute of Technology Shenzhen
Mingyu li
Harbin Institute of Technology Shenzhen
Chunjin Hang
Harbin Institute of Technology
Wenbo Zhu
Harbin Institute of Technology Shenzhen

Research Article

Keywords: vacuum tempered glass, silver paste, low-temperature sintered, microstructure, mechanical strength

Posted Date: March 17th, 2021

DOI: https://doi.org/10.21203/rs.3.rs-299133/v1

Abstract

A low-temperature sintered silver paste was used for metallization on tempered glass to prepare a vacuum tempered glass by soldering with Sn 96.5 Ag 3 Cu 0.5 paste (SAC305). The effects of the glass content and the sintering temperature on the microstructures, shear strengths, and fracture mechanisms of the bondlines were investigated in detail. The microstructure of the thick silver film and its interface with the tempered glass was characterized. The dissolution and precipitation behaviors of the silver in Bi-B-Zn glass were also analyzed. Bi 4 B 2 O 9 crystals were detected in the microstructure of the thick silver film when the joining temperature was increased above 450 °C, which can strengthen the silver film and the interface with the tempered glass. After soldering at 450 °C for 10 min, an excellent bondline was formed with a shear strength of 42.3 MPa and a leak rate of 7.2 × 10 -3 Pa.cm 3 /s by using the low-temperature sintered paste, which had a composition of 80 wt.% silver and 20 wt.% glass powder. Furthermore, heat transfer tests revealed that the vacuum tempered glass had excellent thermal insulation properties. The results showed that the low-temperature sintered silver paste combined with soldering was an effective method to prepare vacuum tempered glass.

1. Introduction

Driven by the requirements of energy conservation, environmental protection and sustainable development, vacuum glass has been{Fang, 2006 #7} widely used in buildings, ship doors and windows, incubators, and airtight seals, which is an important development direction in high-efficiency energy-saving [1-4]. Vacuum glass components have two parallel glass plates with a thickness of about 100 μm, and an array of transparent support columns are required to resist the atmospheric pressure between the glass plates [5,6]. The edges are sealed by glass paste, soft metal solder, or low-temperature sintered silver paste. Then the residual gas is evacuated through the reserved small exhaust port and sealed. The pressure in the vacuum chamber needs to be kept below 0.1 Pa and the overall structure is required to withstand an atmospheric pressure of 10 ton·m^{-2} [7]. One of the most important issues of annealing tempered glass that needs to be considered during this process is the use of sealing materials. To ensure the high strength of tempered glass, it is necessary to reduce the time of the sealing process above 450 °C. However, sealing materials, such as glass solder or soft metals, which could be used to seal the tempered glass either contain lead or require a higher bonding temperature [8]. Lead will harm the human body and the environment. More and more countries and regions have restricted the use of lead [9]. The United Kingdom, the European Union, and Japan have enacted relevant restrictions to explicitly prohibit the use of hazardous substances such as lead in electronics and automobile industries [10,11]. As a consequence, the development of lead-free glass has attracted the attention of many scientific researchers. The development a low-temperature melting lead-free glass sealant for vacuum tempered glass is required. However, using glass solder to seal tempered glass also results in a thermal expansion coefficient mismatch. Heydari reported that a glass-ceramic system, consisting of SiO_2-Al_2O_3-BaO-B_2O_3-CaO, has a thermal expansion coefficient (CTE) of 10.3 × 10^{-6} K^{-1}, which is close to that of solid oxide fuel cells, and the glass adhered well to yttria-stabilized zirconia [12]. Lin used Bi_2O_3-B_2O_3-SiO_2 glass solder to

join the Li-Ti ferrite and nearly defect-free bondlines were obtained under 100 Pa of applied pressure [13]. Also, some researchers have proposed replacing glass solders with low-temperature joining materials (such as metals and resins). However, metal matrix solders (Bi-alloys, Zn-Al based alloys, In-Al based alloys, Au-based alloys, Sn-Zn-Cr alloys) have many limitations because of their poor corrosion resistance and high costs [14-17]. Resins also have disadvantages in impermeability, thermal stability, and aging resistance. In response to this phenomenon, a low-temperature sintered silver paste was prepared by combining the low-temperature meltability of Bi-B-Zn glass and the excellent plasticity of metallic silver. High-quality sealed components could be obtained by preparing a thick layer of silver film on the tempered glass substrate before soldering. The silver paste is a new type of bonding material, which is composed of a conductive phase, a binder phase, and an organic carrier [18-22]. The silver paste was printed on the substrate by screen printing to form a silver paste layer, and after sintering the metallization thick silver film for soldering was obtained [23,24].

In this work, the low-temperature sintered silver paste was used for surface metallization, and the vacuum tempered glass was sealed by soldering. The vacuum tempered glass was prepared with good bondline performance and excellent airtightness. The microstructure and sintering mechanism of the thick silver film were analyzed and the shear fracture mechanism was also clarified. Therefore, the lead-free low-temperature sintered silver paste was combined with soldering as an effective way to prepare vacuum tempered glass, which will replace the leaded glass sealing method.

2. Experimental Procedure

2.1 Materials

The Bi-B-Zn glass was synthesized using bismuth trioxide (AR, ≥ 99.0 %), boric acid (AR, ≥ 98.0 %), zinc oxide (AR, ≥ 99.0 %) which were purchased from Aladdin®, Shanghai, China. The submicron silver powder was purchased from Changsha Tianjiu Metal Co., Ltd, Changsha China. Other raw materials were purchased from Aladdin®, including ethyl celluloses, soy lecithin, ethyl acetate (AR, ≥ 99 %), defoamer, 1,2-propanediol, (AR, ≥ 99 %) and terpineol (AR, ≥ 95 %).

2.2 Preparation of the silver paste

The low-temperature sintered silver paste was prepared by mixing silver powder, Bi-B-Zn glass powder, and an organic vehicle (ethyl cellulose, soy lecithin, ethyl acetate, antifoaming agent, 1,2-propanediol, and terpineol) with the ratio of 71:18:11 (wt. %) using a planetary gravity mixer. The organic additives were used to disperse the solid powder and change the rheological properties of the low-temperature sintered silver paste.

2.3 Sample preparation process

The low-temperature sintered silver paste was printed on tempered glass surfaces, with a size of 20 mm × 20 mm × 4 mm and 10 mm × 10 mm × 4 mm. The size of the pattern for tempered glass surfaces

metallization with the silver paste was 2 mm × 2 mm × 20 μm. The excess organic solvent was removed, and the thick silver film was obtained after the sintering process was carried out in a rapid heating slide furnace at 430 °C, 450 °C, and 470 °C for 10 min, respectively. Then, a layer of SAC305 was printed on the surface of the prepared silver film, as shown in Fig. 1.

2.4 Characterization

The phase composition of the Bi-B-Zn glass and the products in the brazed tempered glass bondlines were investigated by X-ray diffraction (XRD) using a diffractometer (Rigaku SmartLab D/max2500) with Cu Kα radiation. The Differential Scanning calorimetry (DSC) curves of Bi-B-Zn glass powder and silver paste were recorded using a thermogravimetric analyzer (Netzch TGA STA 449 F3) and a differential scanning calorimeter (Netzch DSC STA 449 F3). The microstructures of and the fracture morphologies of the bondlines were analyzed using a scanning electron microscope (SEM, S4700, Hitachi) equipped with an energy dispersive spectrometer (EDS). The room temperature shear strength was tested using a shear strength teste apparatus (MFM1200-10031311-L). The microstructures and the element distribution in the interface of bondlines were analyzed using a transmission electron microscope (TEM, Tslo F200X) equipped with an energy dispersive spectrometer (EDS). TEM samples were prepared using a focused ion beam (FIB, FEI Scios) and a micro-sampling method. The airtightness of the vacuum tempered glass was evaluated using a helium mass spectrometer leak detector. Test conditions A1: test pressure = 310 kPa, pressurization time = 2 h, test environment conditions = 25 °C and humidity = 50 % RH, pressure = 101 kPa in the corresponding lumen volume: $0.5\ cm^3 \leq V < 1.0\ cm^3$. The eligibility criterion was $\leq 1.0 \times 10^{-2}$ $Pa.cm^3/s$. The test procedure was as follows: the component to be tested was placed in a sealed chamber with helium gas at a predetermined pressure and time, the helium gas adsorbed on the surface was removed after taking out from the chamber, and transferred the component to a helium mass spectrometer leak detector to measure a leak rate. The thermal insulation performance of the vacuum tempered glass was recorded using a temperature sensor.

3. Results And Discussion

3.1 Characterization of Bi-B-Zn glass

To sinter the silver paste at low temperatures, the glass used to prepare the silver paste should preferably be amorphous. The X-ray diffraction pattern of the Bi-B-Zn glass powder is shown in Fig. 2a. There were only two broad peaks and no crystal phase peaks detected, which indicated the Bi-B-Zn glass powder was amorphous. The glass transition temperature (T_g = 353 °C) and the crystallization temperature (T_c = 448 °C) of Bi-B-Zn glass were measured by a DSC analyzer, and are shown in Fig. 2b.

3.2 Preparation and characterization of silver paste

The silver paste was prepared using a planetary gravity mixer by mixing Bi-B-Zn glass powder, silver particles, and an organic carrier with a ratio of 17:69:14 (wt. %). Different organic additives were used to disperse the glass powder and the silver particles and to modify the rheological properties. Terpineol

($C_{10}H_{18}O$) was used as a solvent, while ethyl cellulose ($[C_6H_7O_2(OC_2H_5)]n$) was used as a thickener to change the viscosity of the organic carrier for adjusting the rheology and formability of the silver paste; ethyl acetate ($C_4H_8O_2$) was used as a dispersant to ensure that the components in the silver paste were dispersed and mixed evenly, while 1,2-propylene glycol ($C_3H_8O_2$) served as an organic solvent and stabilizer. $C_3H_8O_3$ (GP-330) was used as a defoamer to prevent the generation of bubbles in the silver paste after printing. The specific ratios of the different types of organic additives are given in Table 1.

Table 1 Composition and content of the organic vehicle

Component	$C_{10}H_{18}O$	$[C_6H_7O_2(OC_2H_5)]n$	$C_4H_8O_2$	$C_3H_8O_2$	$C_3H_8O_3$
Content (wt.%)	65.5	3	14.8	9.3	7.4

The DSC and thermogravimetric (TG) analysis of the low-temperature sintered silver paste is shown in Fig. 3. On one hand, the addition of organic carriers with different decomposition and volatilization temperatures played a role in adjusting the viscosity, on the other hand, it could prevent the printed pattern from collapsing due to a large amount of volatilization at a given temperature. The TG curve indicated that the weight of the silver paste had significant decreases at 100 °C, 200 °C, and 300 °C, and remained almost unchanged above 300 °C. Therefore, the debinding process should be carried out in three temperature sections: at 100 °C, 200 °C, and 300 °C held for 60 minutes with a rate of 2.5 °C/min, respectively.

3.3 The microstructure of bondlines

A cross-section image of a typical bondline formed after sintering at 450 °C for 10 min is shown in Fig. 4. The silver film acted as a metallized layer on the tempered glass surface which was tightly bound to the tempered glass, and the tin alloy solder layer (SAC305) was between the two silver film layers. The following work will focus on the interface and sintering behavior of the thick silver film.

The cross-section images of the bondlines with different glass content (wt. %) sintered at 450 °C for 10 min are shown in Fig. 5. Two clear interfaces were observed between the silver film and the SAC305 solder Fig. 5(a), and between the silver film and the tempered glass substrate Fig. 5(d). The results indicated that the glass was crucial for the interfacial bonding between the silver film and the tempered glass substrate, and between the silver film and the SAC305 solder. The silver film was tightly bound to the tempered glass substrate and there was no separation at the interface with either 40 wt.% or 30 wt.% glass content. More glass exposure on the silver film surface caused a non-wetting of the SAC305 solder and the silver film, which led to the separation of the silver film and the SAC305 solder interface Fig. 5(a). Compared with the silver films with either 20 wt.% or 10 wt.% glass content, the transition layer was not noticeable, and the interdiffusion of silver and tin was hindered by a large amount of glass. Although the wettability of the SAC305 solder on the silver film was good and a transition layer was formed, there were

some non-connected holes in the silver film, because it was difficult for the glass to fill these holes. Due to the smaller amount of glass flowing to tempered glass, there was an obvious interface separation between the silver film and the tempered glass with only 10 wt.% glass content Fig. 5(d). This seriously degraded the interface bonding between the silver film and the tempered glass substrate. In summary, the glass content greatly affected the density of the sintered silver film and the bonding strength with the tempered glass substrates. Due to the presence of the glass, silver microparticles were rearranged during the glass softening process. The silver microparticles were not only used in solid-phase sintering, but also diffused through grain boundaries to form a sintered neck. The glass also promoted the sintering of the silver microparticles and molten glass penetrated the gap between the sintering necks through capillary action.

Although the glass content was relatively small, the dissolution in glass and the precipitation process of the silver particles could promote sintering and accelerate the densification process [25,26]. To confirm that silver could dissolve in the Bi-B-Zn glass and precipitate out during the cooling process, the microstructure of the sample was further analyzed by SEM and TEM. There were nanoscale microparticles on the silver film surface. The high-angle annular dark field (HAADF) image near the interface between the glass and silver microparticles, and the elemental distributions of Ag and Bi are shown in Fig. 6. The silver particles gradually sintered together and grew larger during the sintering process. There were no nano-sized silver particles observed in the original material. However, some nanoparticles were detected on the silver film, so this result indicated that the silver dissolved into the glass and nanocrystals precipitated. It could be inferred that silver dissolved into the Bi-B-Zn glass during sintering and penetrated into the glass grid microstructure. Then, the silver dissolved in the glass and precipitated in a supersaturated state and finally formed silver nanoparticles on the surface of the glass during the cooling process. The silver diffused into the liquid glass and the precipitation process could accelerate the diffusion rate of the silver, which was equivalent to accelerating the sintering growth process of the silver microparticles. The mixed solid and liquid phase sintering process could be divided into three steps: (1) Formation of the liquid phase and rearrangement of particles: the glass softened and the liquid phase formed when the glass powder was heated to the softening temperature. The silver particles were mostly suspended within the liquid phase and moved collectively with the help of the surface tension of the liquid phase; (2) Solid-phase sintering and liquid-phase filling: the contact of the silver particles with each other through diffusion sintering, gradually formed a sintered neck and grew, and finally sintered into a massive silver layer. The molten glass filled some voids because of capillary action and its fluidity, thereby the microstructure of the thick silver film rapidly densified; (3) Dissolution and reprecipitation of the solid phase: the angular and convex portions on the silver particles' surfaces preferentially dissolved into the molten glass. Then the supersaturated silver ions in the molten glass precipitated during the cooling process, and the nanocrystalline silver particles reached the silver particles and accelerated the growth of the silver microparticles.

The interface between the glass and the tempered glass, along with the interface between the silver and the glass were characterized by TEM, as shown in Fig. 7. The high angle annular dark-field (HAADF) TEM image of the silver film sintered at 450 °C for 10 min is shown in Fig. 7(a). The EDS element mappings of

the Bi, Zn, Ag, O, and Si elements are shown in Fig. 7(b-f), and Fig. 7(g-h) show the diffraction patterns of regions A and B shown in Fig. 7(a), respectively. The amorphous ring of region A indicated that the glass had an amorphous structure with a low degree of a local order near the substrate surface. The bright Bi-rich region indicated that the $Bi_4B_2O_9$ phase (PDF # 70-1458) was crystal structure, which agreed well with the XRD results shown in Fig. 8. According to the crystallization temperature of 448 °C from the DSC analysis, $Bi_4B_2O_9$ crystals precipitated during sintering process when the temperature was above 450 °C. The nucleation and growth of $Bi_4B_2O_9$ were mainly by diffusion and aggregation of the corresponding elements during the cooling process. Thermal convection with the external environment and the transition of the glass phase to crystalline could provide enough energy for the crystallization process. The precipitation of an appropriate amount of crystalline phase contributed to the strengthening of the overall structure of the thick silver film, which also explained why the sample had the highest shear strength under the process of heating at 450 °C for 10 min.

3.4 The bonding mechanism

The bright-field image and the high-resolution image of region A are shown in Fig. 9(a) and (c). The diffusion of Si, Zn, Bi, and O at the glass and tempered glass substrate interfaces were measured using scanning line B, as shown in Fig. 9(b). It could be seen that the diffusion layer from the glass into the tempered substrate was about 40 nm. The element diffusion curves clearly showed that the content of Bi, Zn, and O changed slowly at the interface. However, the Si content reduced sharply, which could be concluded that the Si remained stable in the glass matrix, but Bi diffused into the tempered glass substrate, indicating an excellent bond was formed at the interface. A large amount of fine $Bi_4B_2O_9$ grains precipitated at the interface and inhibited grain growth, because of the large nucleation energy exchange and consumption in the supercooled glass and the tempered glass substrate. The supercooled melt and a large number of nucleation sites were provided with the help of the surface. More fine nano-grains were formed because of the high cooling rate. Thermal convection and heat exchange provided the energy for the transition process from the amorphous at the interface to crystalline, thus promoting the continuous nucleation of nanocrystals. The X-ray diffraction pattern of the interface was composed of a diffractive halo and a polycrystalline ring, indicating that the interface was mainly composed of a glass phase and a large number of $Bi_4B_2O_9$ grains. After the Bi diffused, which aggregated at the interface and broke through the nucleation barrier, a large number of $Bi_4B_2O_9$ nanocrystals were generated and distributed evenly throughout the interface. A diffusion bond was formed between the glass substrate and the silver film. The precipitation of small grains could hinder the crack propagation in the glass and played a vital role in dispersion strengthening, thereby inhibiting the occurrence of fracture modes at the interface during shear fracture processes, which will greatly increase the adhesion and shear strength of the sintered silver film.

The fracture mode was mainly brittle fracture when glass content was 40 wt.%, as shown in Fig. 10(e). The cracks mainly extended along the inside of the glass or the surface of the tempered glass substrate because the silver particles were separated by large glass resulted in relatively low sintering dense. More

glass existed at silver film and tempered glass substrate interface weakened silver particles on inhibiting crack propagation, which resulted in a low bonding strength of 14.8 MPa. The silver film was well bonded to the tempered glass substrate with 30 wt.% glass content, as shown in Fig. 10(b). Silver particles were peeled off from the glass in the fracture interface and the large brittle fracture mode disappeared. The crack expanded from the glass inside when the tip of the crack met the silver particles, so that the crack penetrated the silver film along the weakest part, and the shear strength could reach 30.1 MPa. Since the glass content in the thick silver film was high, the overall thick silver film still exhibited a certain degree of brittleness, but the silver particles were not separated in the glass, and some silver particles had been sintered to form a whole. The maximum shear strength of 42.3 MPa was obtained with 20 wt.% glass content. The silver film and the tempered glass substrate were well bonded and most of the silver particles were peeled from the glass, as shown in Fig. 10(c). Without a large brittle fracture formed, and visible bowl-shaped structure on the tempered glass substrate surface. The silver particles were sintered well and the gap between them was filled with glass solder, which promoted the bonding force between the silver film and tempered glass substrate. However, the shear strength had the lowest value of 12.8 MPa with 10 wt.% glass content. There was not enough molten glass solder to fill the interface between the silver film and the tempered glass substrate, which resulted in a lot of holes and left an interface that was not fully bonded, as shown in Fig. 10(d). A small amount of glass which existed at the interface was not enough to ensure that the Bi-B-Zn glass presented evenly at all interfaces, which meant that not all fracture interfaces had a bowl-shaped structure, which was described by Fig. 10(h).

One of the most important performance metrics of vacuum tempered glass is airtightness. Good air tightness and internal getter could maintain a high vacuum of the vacuum layer for a long duration. This experiment used the GJB 548B-2005 method 1014.2 test condition A1 (fine leak detection) to test the gas leakage rate of the seal component, as shown in Fig. 11(a). The leak rate was 7.2×10^{-3} Pa.cm^3/s with 80 wt.% Ag silver paste sealed at 450 °C for 10 min. The single-layer glass, double-layer glass, hollow glass component, and tempered vacuum glass component were placed on a 200 °C heating table for the experiment. The temperature of the upper surface was measured with time and plotted, as shown in Fig.11(b). The experimental results showed that the heat transfer of the single-layer glass was the fastest, and the thermal equilibrium could be reached in 5 minutes, at a temperature of 200 °C. Due to the heat dissipation from the surroundings and the upper surface to the environment, the final upper surface temperature was maintained at 144.5 °C. When the double-layer glass and the hollow glass component were selected for the experiment, the heat transfer rate decreased significantly. Thermal equilibrium was reached in 15 minutes and the temperatures were 115.1 °C and 108.5 °C, respectively. However, the gas heat conduction and convection heat transfer were negligible since the middle layer was close to the vacuum in the vacuum glass component. The experimental results also showed that the tempered vacuum glass components reached a thermal equilibrium temperature of 82.5 °C after 24 minutes, which had good thermal insulation performance since the main heat conduction mode was radiant heat transfer. Therefore, these results indicated that the vacuum glass components exhibited excellent thermal insulation performance, compared to hollow glass and other glass structures.

4. Conclusions

A metallization layer was prepared on the tempered glass surface by sintering a silver paste with 80 wt.% silver content and 20 wt.% Bi-B-Zn 20glass content at 450 °C for 10 min. $Bi_4B_2O_9$ crystals precipitated and a large number of small grains formed at the interface at 450 °C, strengthening the thick silver film and enhancing its bonding with the tempered glass substrate. The dissolution and precipitation process of the silver particles in the Bi-B-Zn glass accelerated the diffusion of Ag and promoted the sintering and growth of silver particles. The silver particles were peeled from the glass as the main shear fracture mechanism, and its bonding force with the tempered glass substrate was up to 42.3 MPa. The leak rate of 7.2×10^{-3} $Pa.cm^3/s$ and excellent thermal insulation performance were obtained using the low-temperature sintered silver paste combined with soft soldering.

Declarations

AUTHOR INFORMATION

Corresponding Author

*E-mail addresses: zhuwenbo@hit.edu.cn

Declaration of competing interest

The authors declare that they have no known competing financial interests or personal relationships that could have appeared to influence the work reported in this paper.

Acknowledgment

The authors acknowledge the Shenzhen Science and Technology Plan (No. JCYJ20190806143814935), the Science and Technology Innovation Committee of Shenzhen (JCYJ20180306172006392), the State Key Laboratory of Advanced Welding and Joining, Harbin Institute of Technology (AWJ-21M07), the Key Laboratory on Reliability and Environmental Engineering Technology (JZX7Y201911SY000401-6142004190202) and National Natural Science Foundation of China (No.52075125).

References

1. R. E. Collins, T. M. Simko, Current status of the science and technology of vacuum glazing(J). Sol. Energy. 62,(3), 189-213 (1998)
2. Y. Fang, P. C. Eames, B. Norton et al., Experimental validation of a numerical model for heat transfer in vacuum glazing(J). Sol. Energy. 80,(5), 564-577 (2006)
3. E. Cuce, P. M. Cuce, Vacuum glazing for highly insulating windows: Recent developments and future prospects(J). Renewable and Sustainable Energy Reviews. 54 1345-1357 (2016)

4. P. C. Eames, Vacuum glazing: Current performance and future prospects(J). Vacuum. 82,(7), 717-722 (2008)
5. L. Jun, Z. Min Hong, Study on the Properties and Manufacturing Technology of Vacuum Plate Glass(J). Equipment Manufacturing Technology,(12), 165-167 (2014)
6. Z. W. Xu, H. Wang, International third-generation energy-saving door and window glass low-emission flat vacuum glass(J). Resources and Development,(4), 42-44 (2005)
7. J. Tang, W. Xu, Present status of vacuum glass industrialization(J). Bulletin Chinese Ceramic Society. 34 56-61 (2015)
8. Y. Jin, Z. Lei, X. Tong et al., Research Progress on Recycling Technology of Lead-containing Glass in Waste Cathode Ray Tubes(J). IOP Conference Series: Earth and Environmental Science. 446 22047 (2020)
9. Q. Sun, W. Yang, Y. Liu et al., Microstructure and mechanical properties of tempered glass joint bonded with Bi-B-Zn low melting glass(J). J. Mater. Process. Tech. 271 404-412 (2019)
10. G. H. Hwang, W. Y. Kim, H. J. Jeon et al., Physical Properties of Barrier Ribs of Plasma Display Panels: II, Effects of Fillers(J). J. Am. Ceram. Soc. 85,(12), 2961-2964 (2002)
11. T. Naito, T. Aoyagi, Y. Sawai et al., Lead-Free Low-Melting and Semiconductive Vanadate Glass Applicable to Low-Temperature Sealing(J). Jpn. J. Appl. Phys. 50,(8), 88002 (2011)
12. F. Heydari, A. Maghsoudipour, Z. Hamnabard et al., Evaluation on Properties of CaO–BaO–B2O3–Al2O3–SiO2 Glass–Ceramic Sealants for Intermediate Temperature Solid Oxide Fuel Cells(J). J. Mater. Sci. Technol. 29,(1), 49-54 (2013)
13. P. Lin, T. Lin, P. He et al., Investigation of microstructure and mechanical property of Li–Ti ferrite/Bi2O3–B2O3–SiO2 glass/Li–Ti ferrite joints reinforced by FeBi5Ti3O15 whiskers(J). J. Eur. Ceram. Soc. 35,(9), 2453-2459 (2015)
14. V. Chidambaram, J. Hattel, J. Hald, High-temperature lead-free solder alternatives(J). Microelectron. Eng. 88,(6), 981-989 (2011)
15. Y. Fang, T. J. Hyde, F. Arya et al., Indium alloy-sealed vacuum glazing development and context(J). Renewable and Sustainable Energy Reviews. 37 480-501 (2014)
16. S. Kim, K. Kim, K. Suganuma et al., Interfacial Reactions of Si Die Attachment with Zn-Sn and Au-20Sn High Temperature Lead-Free Solders on Cu Substrates(J). J. Electron. Mater. 38,(6), 873-883 (2009)
17. G. Zhao, G. Sheng, J. Luo et al., Solder Characteristics of a Rapidly Solidified Sn-9Zn-0.1Cr Alloy and Mechanical Properties of Cu/Solder/Cu Joints(J). J. Electron. Mater. 41,(8), 2100-2106 (2012)
18. D. Burnat, P. Ried, P. Holtappels et al., The Rheology of Stabilised Lanthanum Strontium Cobaltite Ferrite Nanopowders in Organic Medium Applicable as Screen Printed SOFC Cathode Layers(J). Fuel CellsNA-NA (2009)
19. M. R. Somalu, V. Yufit, I. P. Shapiro et al., The impact of ink rheology on the properties of screen-printed solid oxide fuel cell anodes(J). Int. J. Hydrogen Energ. 38,(16), 6789-6801 (2013)

20. S. Murakami, K. Ri, T. Itoh et al., Effects of ethyl cellulose polymers on rheological properties of (La,Sr)(Ti,Fe)O3-terpineol pastes for screen printing(J). Ceram. Int. 40,(1), 1661-1666 (2014)
21. S. P. Wu, Q. Y. Zhao, L. Q. Zheng et al., Behaviors of ZnO-doped silver thick film and silver grain growth mechanism(J). Solid State Sci. 13,(3), 548-552 (2011)
22. J. Tsai, S. Lin, Silver powder effectiveness and mechanism of silver paste on silicon solar cells(J). J. Alloy. Compd. 548 105-109 (2013)
23. Y. Li, W. Gan, J. Zhou et al., Glass frits coated with silver nanoparticles for silicon solar cells(J). Appl. Surf. Sci. 341 127-133 (2015)
24. A. S. Ionkin, B. M. Fish, Z. R. Li et al., Screen-Printable Silver Pastes with Metallic Nano-Zinc and Nano-Zinc Alloys for Crystalline Silicon Photovoltaic Cells(J). ACS Appl. Mater. Inter. 3,(2), 606-611 (2011)
25. D. Kim, S. Shim, S. Hwang et al., Electrical Properties of Screen Printed Silicon Solar Cell Dependent upon Thermophysical Behavior of Glass Frits in Ag Pastes(J). Jpn. J. Appl. Phys. 48,(5), 5 (2009)
26. S. Yao, J. Xing, J. Zhang et al., Microscopic investigation on sintering mechanism of electronic silver paste and its effect on electrical conductivity of sintered electrodes(J). Journal of Materials Science: Materials in Electronics. 29,(21), 18540-18546 (2018)

Figures

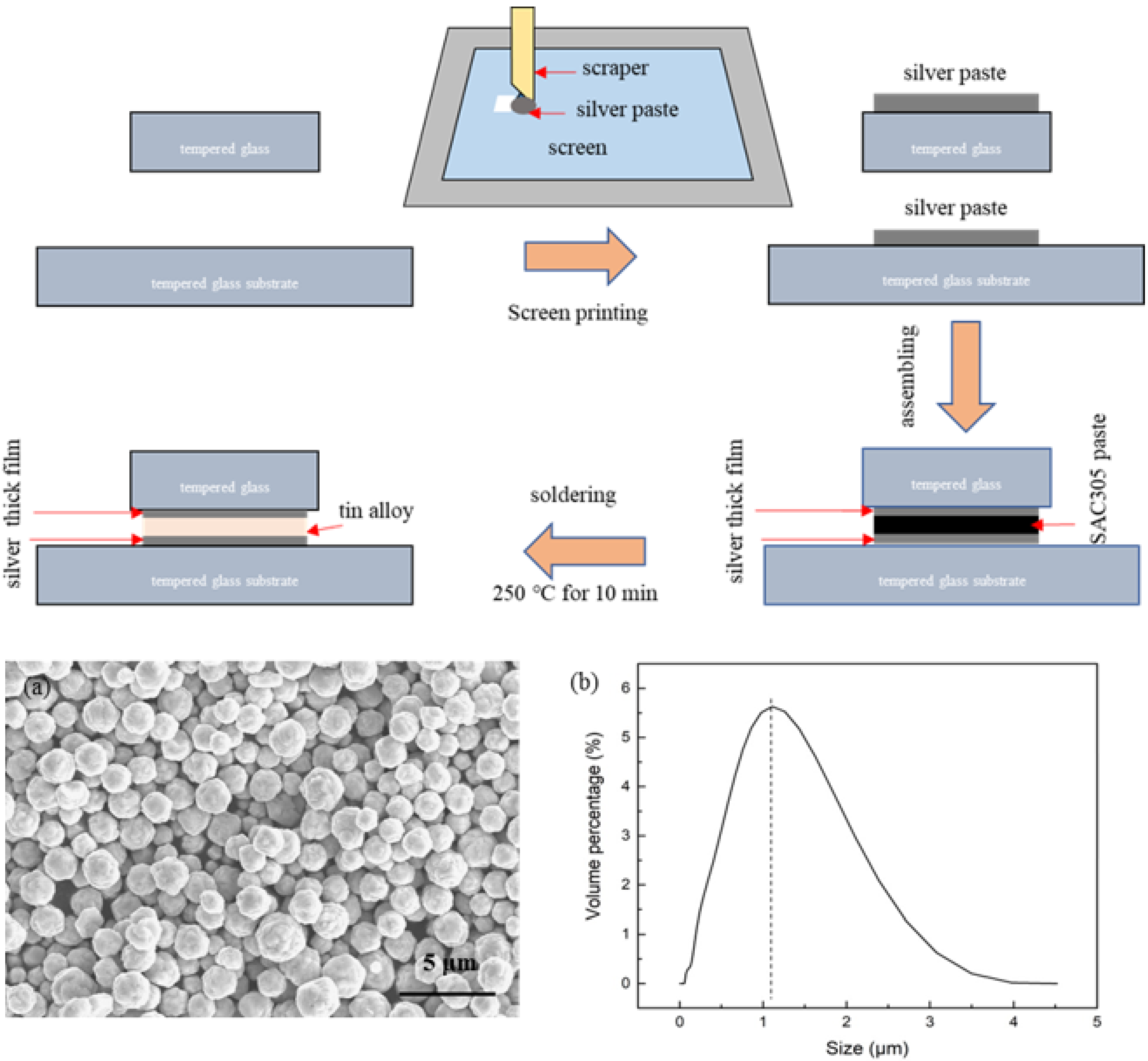

Figure 1

The joining process of tempered glass components.

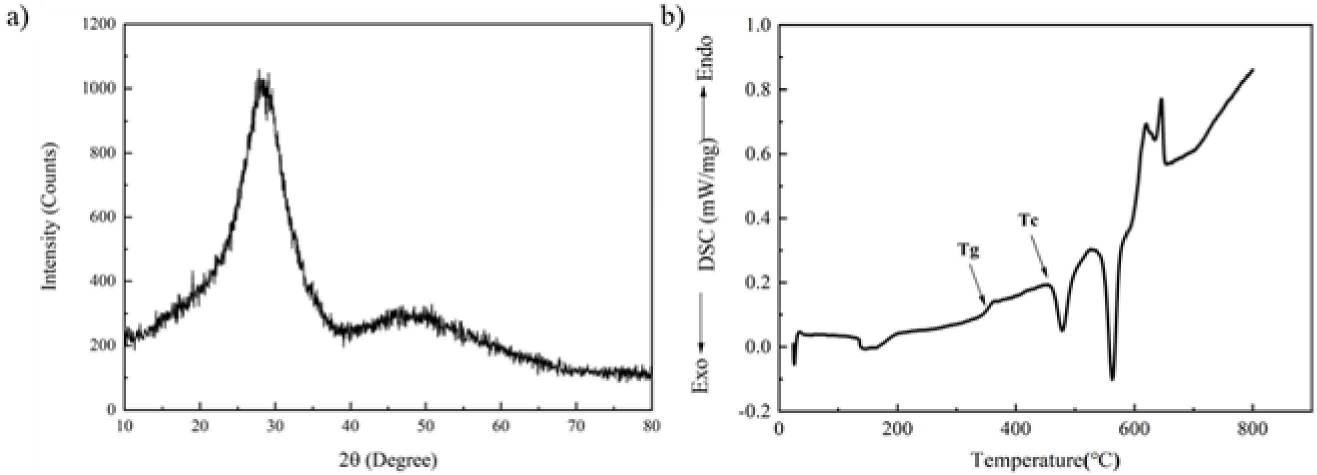

Figure 2

Characterization of the Bi-B-Zn glass: (a) XRD pattern; (b) DSC curve.

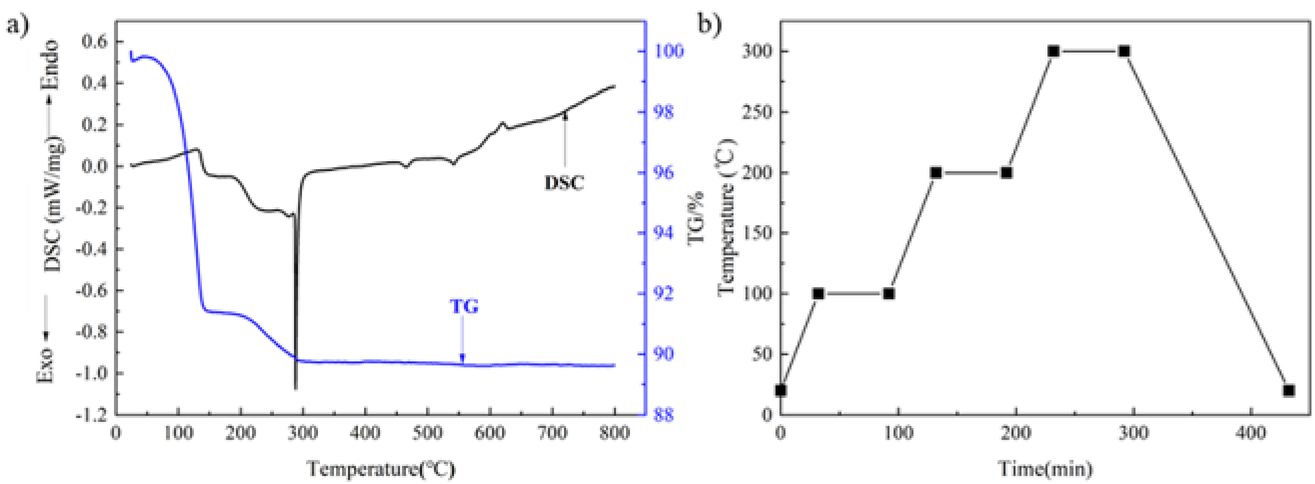

Figure 3

(a) The TGA/DSC curves of the silver paste; (b) the curves of the debinding process.

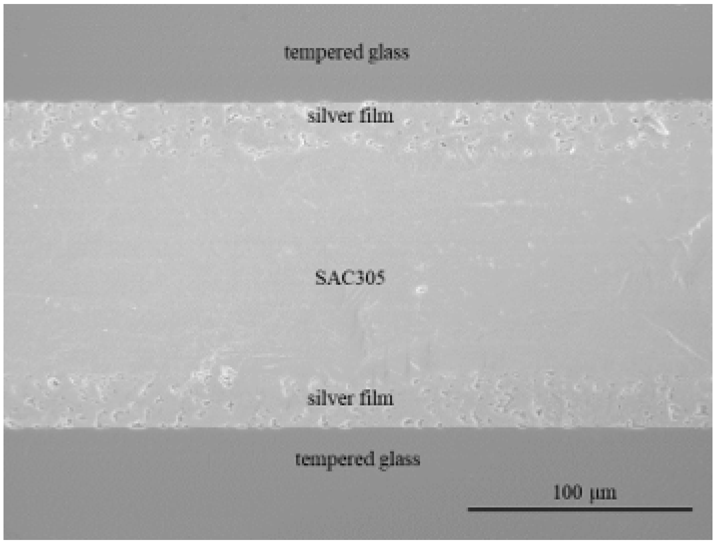

Figure 4

SEM cross-section image of a bondline.

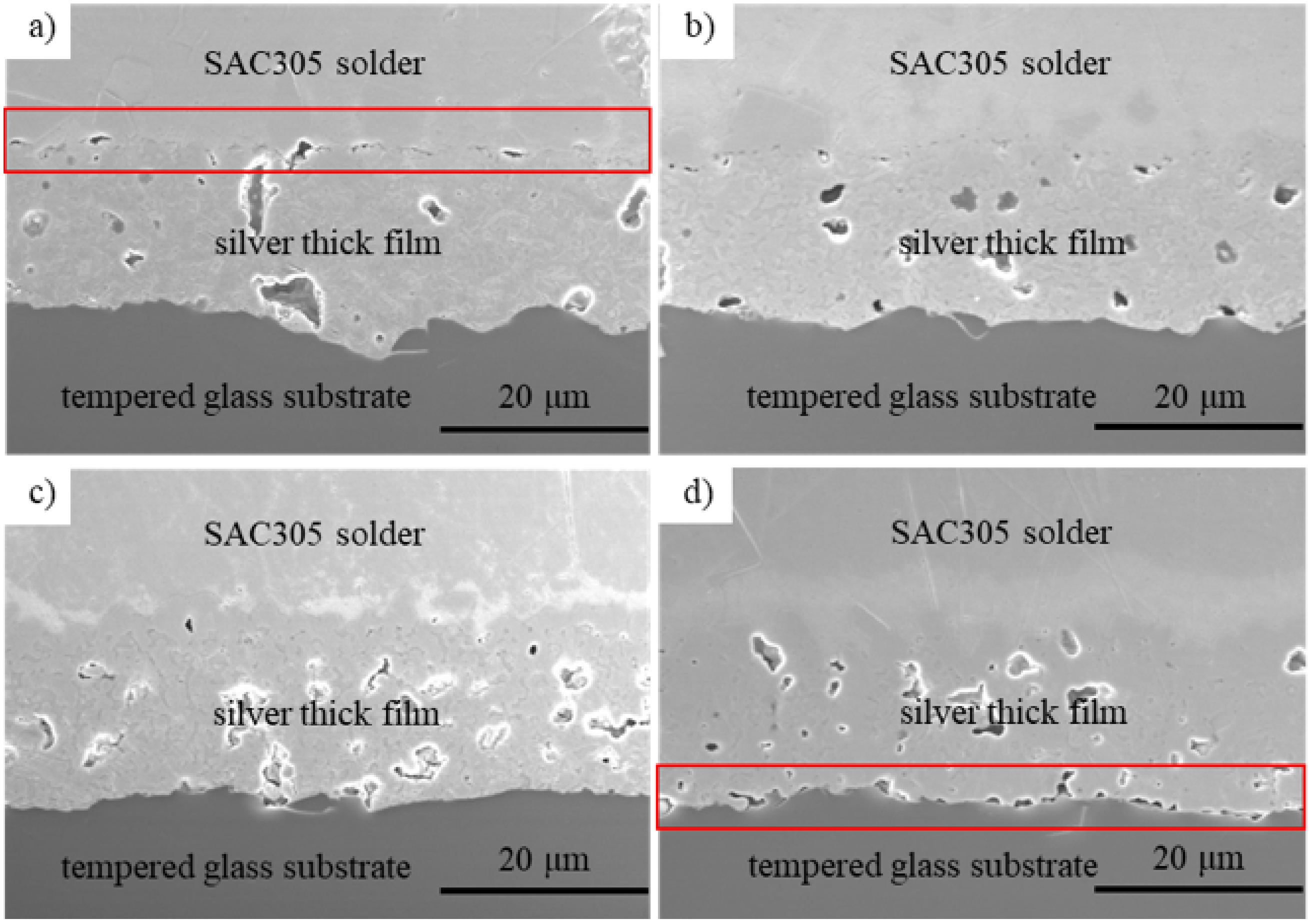

Figure 5

SEM cross-section images of the bondlines with different glass content (wt. %) sintered at 450 °C for 10 min: a) 40%; b) 30%; c) 20%; d) 10%.

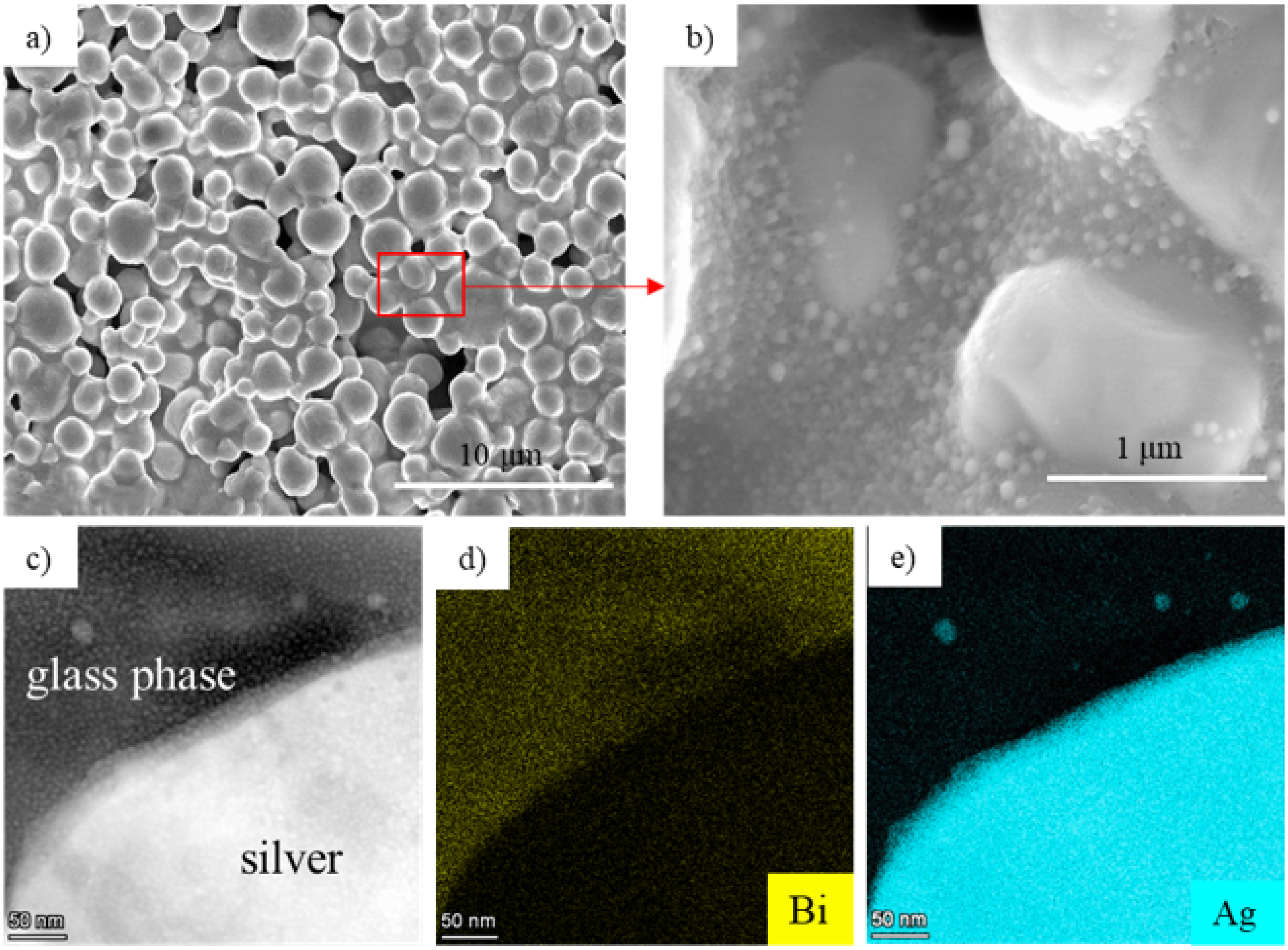

Figure 6

TEM image and EDS element mapping of Ag and glass interfaces: a-b) silver film; c) HAADF image; d) Bi, and e) Ag element distribution map.

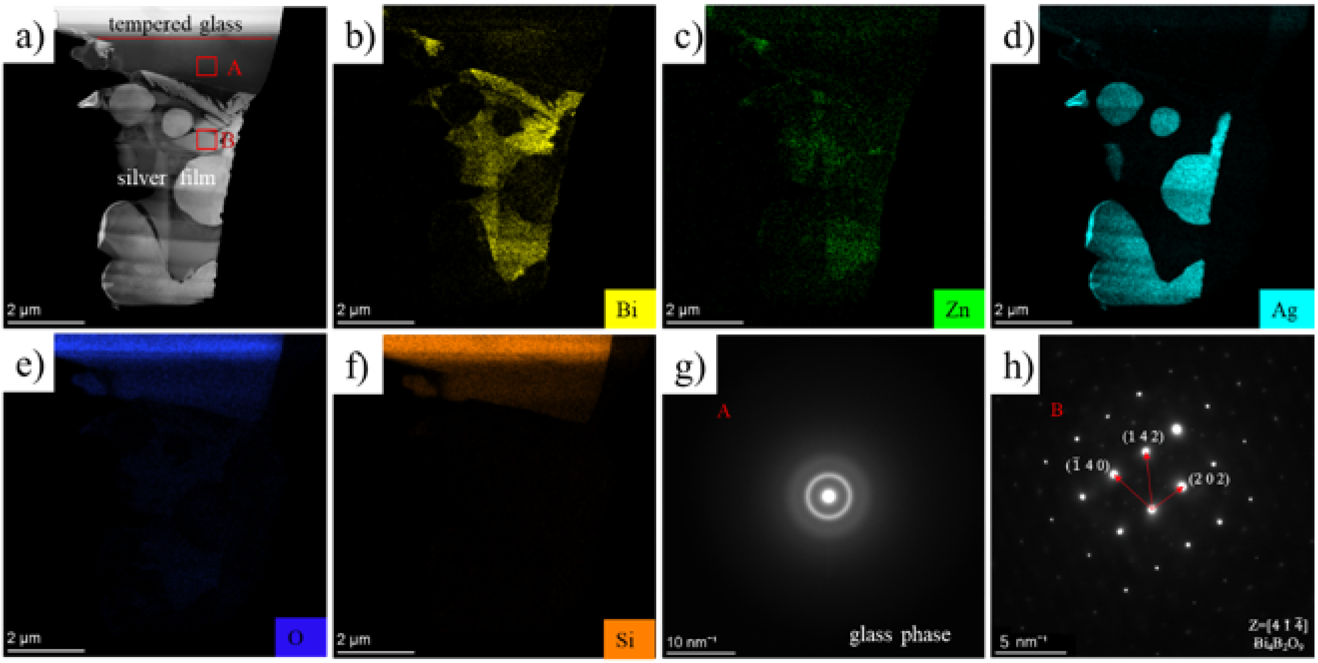

Figure 7

TEM images of a precipitated crystal: a) HAADF image; b-h) distributions of Bi, Zn, Ag, O, Si elements; g) the electron diffraction patterns of regions A and B, shown in (a).

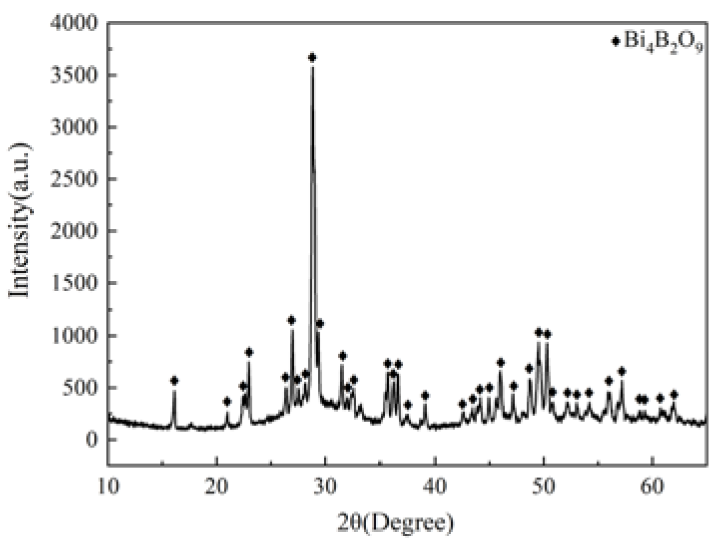

Figure 8

XRD pattern of Bi-B-Zn glass sintered at 450 °C for 10 min.

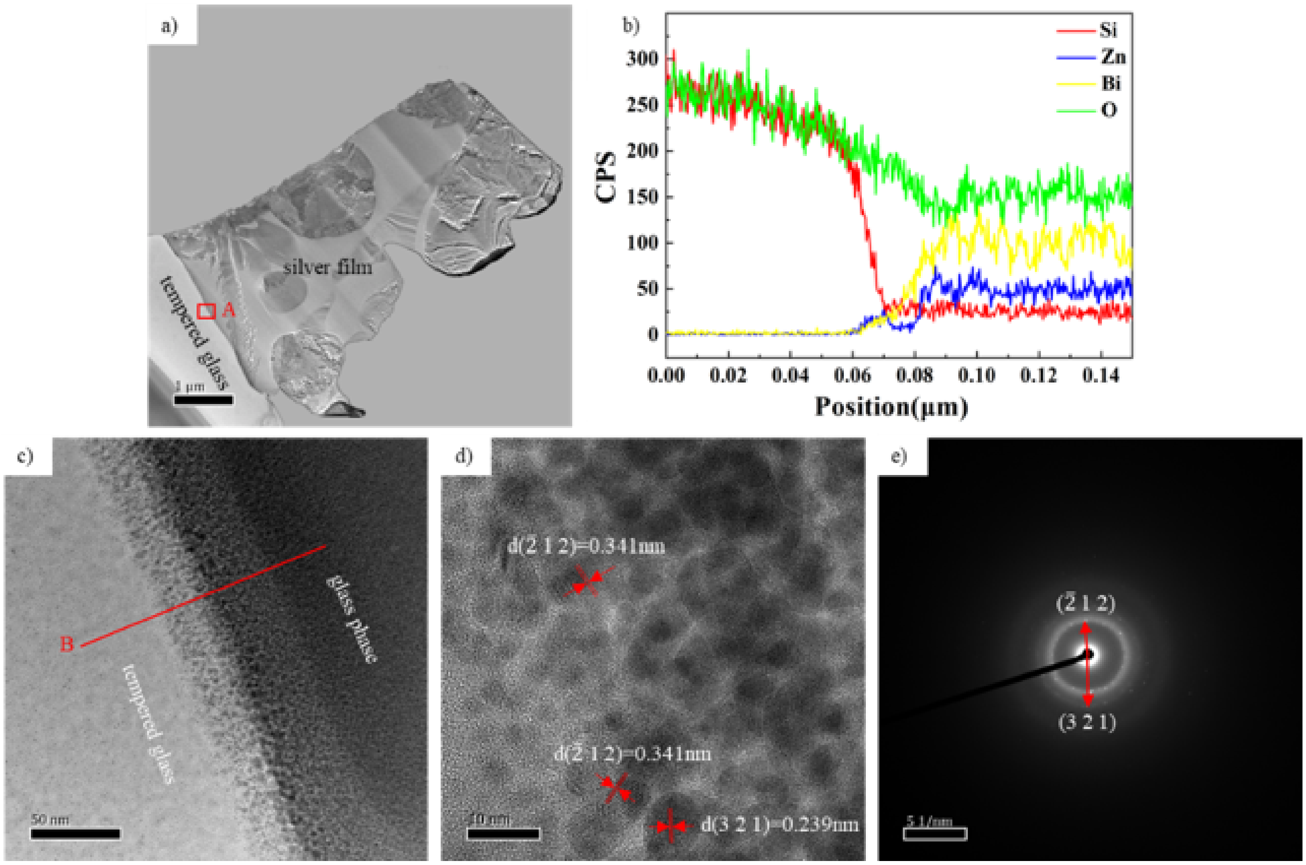

Figure 9

TEM images of the interface between Bi-B-Zn glass and tempered glass: a) bright-field image; b) elemental diffusion line scan curves along line B in shown in (c); c-d) high-resolution images of the interface; e) selected electron diffraction pattern at the interface.

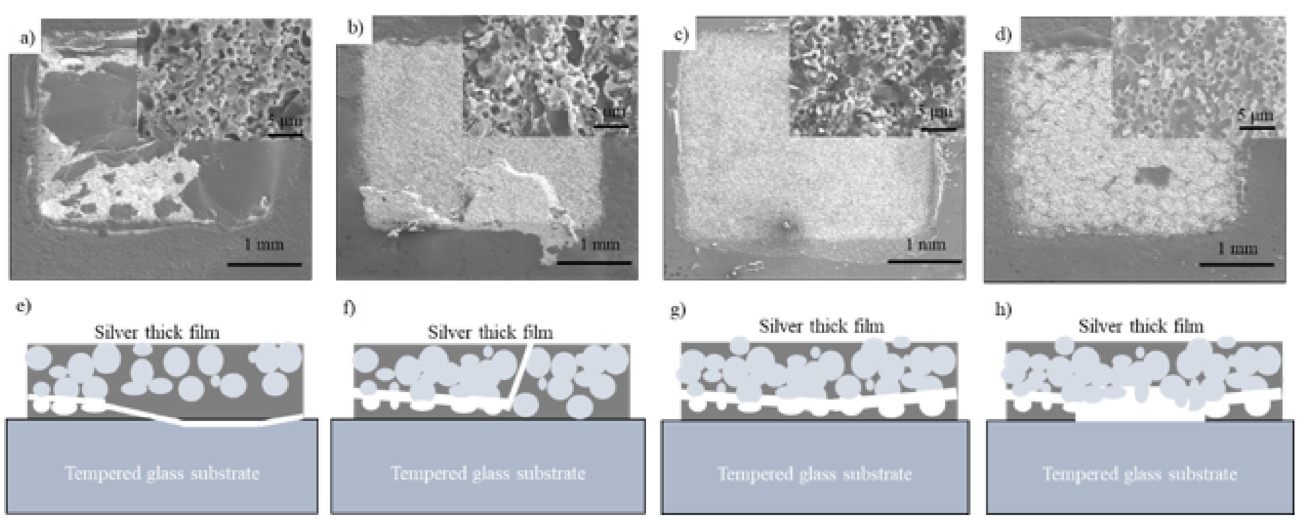

Figure 10

Fracture interfaces and fracture modes of different glass contents (wt. %): a) and e) for 40 wt.%; b) and f) for 30 wt.%; c) and g) for 20 wt.%; d) and h) for 10 wt.%.

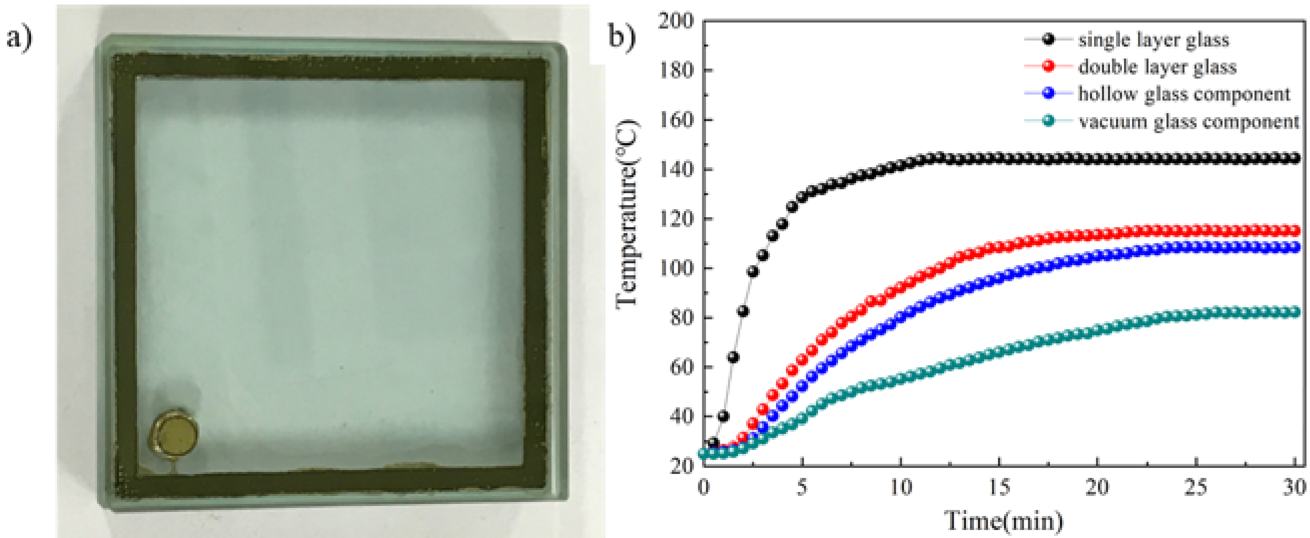

Figure 11

Vacuum tempered glass component and insulation curves.